The Time-Dependent Hydraulic Flow and Dissipation over the Sill of Observatory Inlet

MICHAEL W. STACEY* AND LEN J. ZEDEL**

Institute of Ocean Sciences, Sidney, B.C. Canada V8L 4B2

(Manuscript received 29 March 1985, in final form 20 December 1985)

ABSTRACT

The time-dependent hydraulic flow over the sill of a tidally energetic fjord, Observatory Inlet, British Columbia, is studied. Acoustic observations of streamlines and velocity were made near the sill crest during the summer of 1982, a time when freshwater runoff into the inlet had created a distinct surface layer. While the tide is accelerating, a simple, three-layer, hydraulic model accurately simulates the flow near the sill crest. However once the tide begins decelerating the observed flow undergoes a transition which the three-layer model cannot explain.

It is estimated that during the period of observation the hydraulic flow utilized only about 5% of all the energy removed from the barotropic tide. This suggests that other processes, such as the internal tide, are removing most of the energy from the barotropic tide.

1. Introduction

The tidally driven motion in the vicinity of underwater sills can be very nonlinear and result in considerable mixing, as observed, for example, in Massachusetts Bay (Haury et al., 1979), Knight Inlet (Farmer and Smith, 1980), Puget Sound (Geyer and Cannon, 1982), and Observatory Inlet (Farmer and Freeland, 1983). In this paper the tidal flow in Observatory Inlet, a fjord located on the coast of British Columbia, is analyzed.

Many theoretical analyses do not allow for the dissipation of energy and so are inadequate when it comes to describing flows in which mixing processes are important. One common theoretical method for studying steady, inviscid, nonlinear flows over sills involves using special upstream conditions that reduce the problem to linear form. Often, it is assumed that all of the streamlines originate upstream of the sill and that the upstream density gradient is linear. This method has been used, for example, by Long (1953, 1955), Drazin and Moore (1967), Miles (1968), Miles and Huppert (1968, 1969) and Huppert and Miles (1969), and has proved to be reasonably accurate in describing the lee-wave field downstream of the sill. However, the experiments of Davis (1969) on flows of this type have shown that the total drag on the sill can be much greater than the wave drag predicted by this theory. That is, from an energetic point of view, sill processes such as hydraulic jumps and boundary layer separation are often more important than the lee waves.

Nonlinear sill flows can also be analyzed by solving the nonlinear, shallow water equations. These equations are hydrostatic and so lee waves cannot be part of the solution, but hydraulic transitions, i.e., hydraulic jumps, in the vicinity of the sill can be readily analyzed. A number of studies, e.g., Long (1954), Yih and Guha (1955), Houghton and Kasahara (1968) and Houghton and Isaacson (1970), have shown the usefulness of this method for analyzing hydraulic flows.

Acoustic observations of streamlines and water velocity taken in Observatory Inlet (Fig. 1) during the summer of 1982 suggest that there is intense mixing in the hydraulic jumps that occur downstream of the sill. The energy driving these flows is obtained from the barotropic tide, and because of their apparent intensity one might expect them to utilize a large percentage of the total energy extracted from the tide. However, a calculation by Stacey (1984), which ignores the nonlinear processes occurring near the sill, shows that almost all of the power withdrawn from the barotropic tide in Observatory Inlet can be accounted for by a linear model of the internal tide. Obviously, because the model is linear the influence of nonlinearities on the internal tide could not be taken into account and no estimation of the amount of energy going into nonlinear processes could be made. However, if nonlinear processes do in fact extract a significant amount of energy directly from the surface tide, they may have an important influence on the rate at which energy is fed into the internal tide. Therefore, a major goal of this study was to estimate the amount of energy going into the nonlinear sill processes in Observatory Inlet. This has been done by solving the time dependent, nonlinear, shallow water equations for a tidally driven

* Present affiliation: Department of Oceanography, University of British Columbia, Vancouver, B.C. Canada V6T 1W5.

** Present address: CSIRO Marine Laboratories, Hobart, Tasmania, Australia.

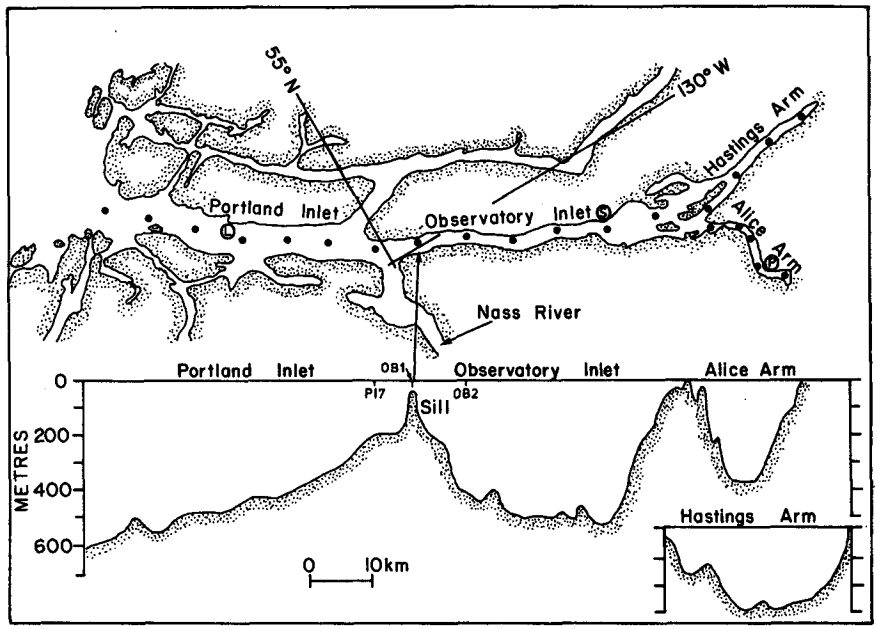

FIG. 1. Plan view and longitudinal section of the inlet system. CTD stations are indicated by the solid circles in the plan view and, for the three stations closest to the sill, by alphanumeric symbols in the longitudinal section. Tide gages are located at Lizard Cove (L), Salmon Cove (S), and Pearson Point (P).

flow over a sill. This method has been used because 1) hydraulic transitions probably dissipate more energy in the inlet than lee waves, and 2) there is a data base to which models of this type of flow can be compared. An interesting analytic, quasi-steady, hydraulic analysis of the flow in Observatory Inlet has recently been developed by Farmer and Denton (1985), but the complementary numerical approach presented here permits more detailed comparisons with the available data, particularly in the lee of the sill where most of the dissipation occurs. Also, by using a time dependent model one can investigate how the temporal variability of the tide influences the structure of the sill flow. A three-layer model predicts that only about 5% of all the energy removed from the barotropic tide is utilized by the hydraulic flow, a result consistent with the calculation of Stacey (1984). Although this result strictly applies to Observatory Inlet, we feel it is rather general and probably applies to other inlets with similar flow characteristics.

A related goal of this study was to determine if the hydrostatic model could simulate the observed streamlines and velocities. They varied significantly during a tidal cycle, and while the tidal velocity is increasing the flow is adequately represented by a three-layer model. While the tidal velocity is decreasing, however, the model fails to reproduce the observed flow, possibly because mixing modified the density gradient of the real flow in such a way that a layered interpretation of the motion became unrealistic.

2. The inlet

Observatory and Portland Inlets (Fig. 1) are located on the coast of British Columbia just south of the Alaska Panhandle. Portland Inlet is about 5 km wide and Observatory Inlet is about 2.5 km wide. The sill which separates the two inlets is located about 50 km from the open ocean. It has an average depth of about 50 m but ranges between 30 and 60 m in depth (Fig. 2).

The major source of freshwater runoff is the Nass River, which flows into Portland Inlet about 5 km from the sill. During the summer months, maximum runoff occurs due to increased meltwater flow (Fig. 3). This large runoff results from a fresh surface layer that is 10 m thick in the region of the sill (Fig. 4).

Observations of the flow evolution over Observatory Inlet sill were made during two ebb tides on 19 and 20 June 1982. The rapidly changing flow field was monitored using acoustic flow visualization and Doppler profiling techniques (Zedel, 1985). A towable profiling CTD was used to record changes in the density structure.

Flow visualization is provided by a 100 kHz echosounder attached to the hull of a ship. As the ship moves along the inlet the echosounder produces images which in many ways are similar to hydrogen bubble photographs: as passive acoustic scatterers such as plankton and temperature inhomogeneities are swept over the sill, they outline motions of the water column. Indi-

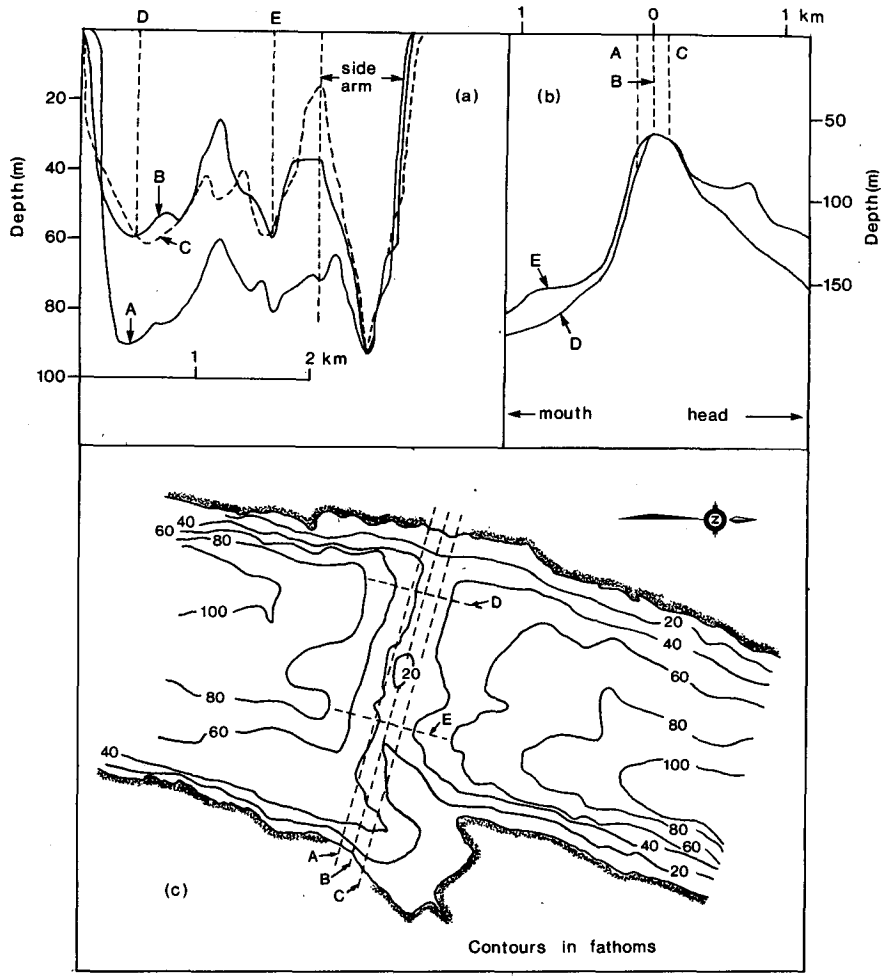

FIG. 2. Cross sections (a), longitudinal sections (b) and plan view (c) of the inlet system near the sill.

vidual scatterers trace out short streamlines that allow an inference of the overall flow regime (Fig. 5).

Remote measurements of flow speed are made with a 215 kHz range gated Doppler probe. This instrument projects acoustic pulses along a narrow beam (1° 3 dB beamwidth) and determines the flow speed along the beam axis from the Doppler shift of the backscattered sound (e.g., see Pinkel, 1980). In collecting the Observatory Inlet data, the acoustic beam was directed down-inlet at 62° below horizontal (Fig. 6). Because of the position of the probe, the velocity in the fresh surface layer was not obtainable. Also, the velocity close to the bottom cannot be accurately determined; in this region contamination of the acoustical signal by reflections off the inlet bottom introduces a bias that cannot easily be removed (Zedel, 1985).

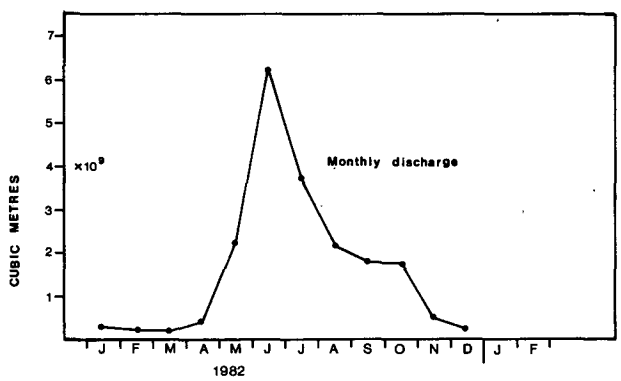

FIG. 3. Monthly freshwater discharge from the Nass River for the year 1982.

Data were collected during traverses of the sill by simultaneously operating the echosounder, the Doppler probe, and towing the CTD at a fixed depth; ship position was monitored with a microwave positioning system. At the end of each sill traverse, a CTD cast was made to provide a density profile.

The observations, which were taken over a relatively

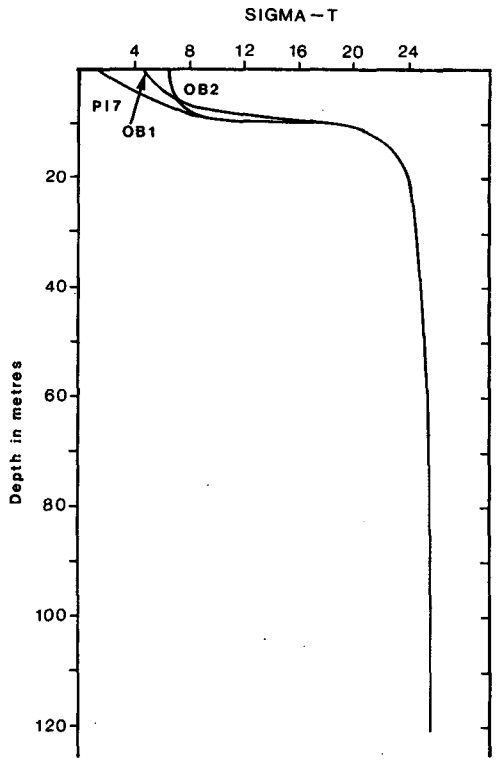

FIG. 4. Sigma-t profiles near the sill during 12 June 1982.

shallow region of the sill during a spring tide, show that the tidally forced flow in the region of the sill is very complex and can exhibit a number of different kinds of motion. Figures 5a and 5b show streamlines typical of Observatory Inlet that were observed during the same tidal cycle shortly before and after maximum tidal velocity. Figure 5c (also Fig. 4c in Farmer and Denton, 1985) shows anomalous streamlines that were observed the following day near maximum tidal velocity. Otherwise the flow that day was similar to the flow in Fig. 5a before maximum tidal velocity and to the flow in Fig. 5b after maximum tidal velocity. One of the most noticeable features of the flow is the finite amplitude lee wave or hydraulic jump that occurs in the lee of the sill. It exists for a major portion of each tidal cycle and appears to be associated with intense mixing. Also, its shape appears to depend on whether the tidal velocity is increasing or decreasing. While the tide is accelerating, the streamlines extend almost horizontally downstream of the sill crest for about 60 m and then abruptly plunge downwards. After maximum tidal velocity, however, the streamlines begin deepening immediately downstream of the sill crest. This leads one to suspect that the response of the flow depends on the rate at which the tidal forcing is changing. One can investigate this possibility with a time-dependent model.

The flow must in some sense be supercritical over the sill before a hydraulic jump can exist. Farmer and Smith (1980) find that the hydraulic response of sill flows can be crudely categorized in terms of the internal Froude numbers

$$F_i = \frac{U_s}{c_i} \tag{1}$$

where U_s is the sectionally averaged flow velocity over the sill crest and c_i the phase speed according to linear theory of the ith internal mode over the sill crest. The sectionally averaged velocity is given by

$$U_s = \frac{S}{A}\frac{d\eta}{dt} \tag{2}$$

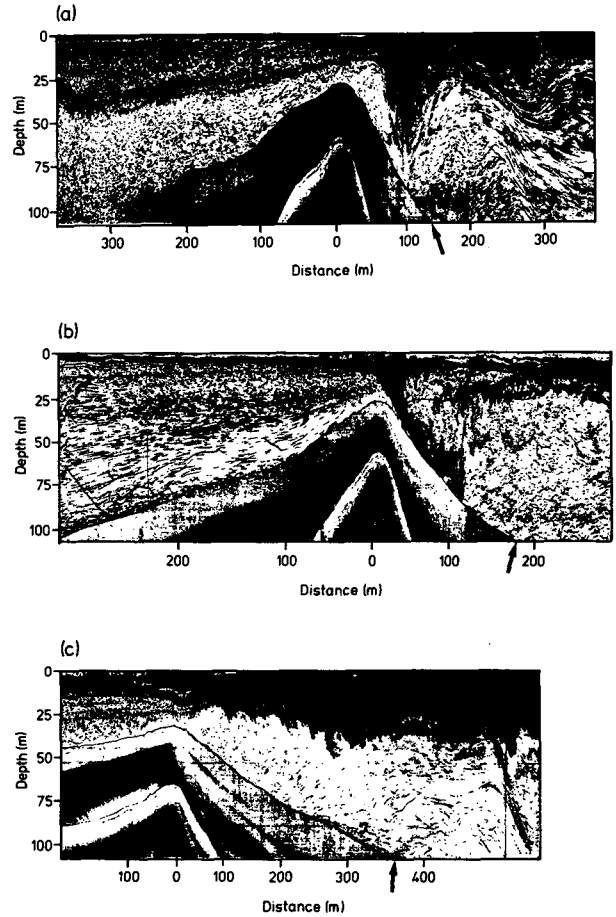

FIG. 5. Streamlines of the ebb tide, (a) 2.8 h after slack tide on 19 June 1982, (b) 3.7 h after slack tide on 19 June 1982 and (c) 3.1 h after slack tide on 20 June 1982. The times given are for when the streamlines at the sill crest were observed. The flow is from left to right towards the mouth of the inlet. In fact, what one is seeing is a plot of the acoustic image versus time. The abscissa has been changed from time to distance by taking into account the speed with which the ship was moving. As a reference, the arrows indicate where the bottom topography intersects the abscissa.

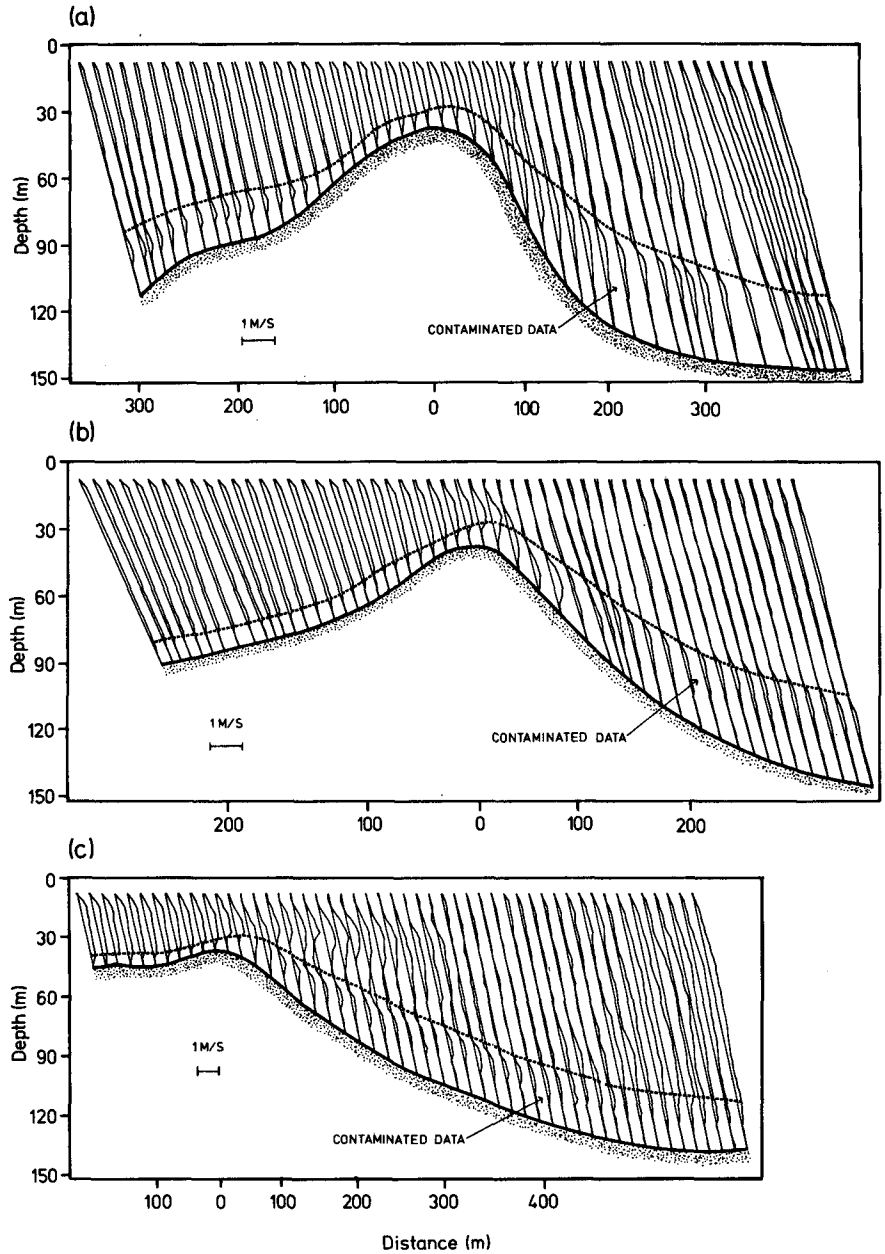

FIG. 6. Profiles of velocity measured along the acoustic beam axis. (The corresponding streamlines are shown in Fig. 5.) The sloped line along which each velocity profile is plotted corresponds to the line of the acoustic beam axis. Flow to the right (left) is indicated by the profile curve being located on the right- (left-) hand side of the reference line. Vertical exaggeration in the figure makes the slope of the reference line appear greater than the 62° below horizontal at which the acoustic beam was directed. Above the dashed line the velocities are accurate to within ±2 cm s^{-1}. Below the dashed line the measurements are biased by reflections off the bottom of the inlet.

where S is the surface area of the inlet landward of the sill, A the cross-sectional area of the inlet over the sill crest, and η the tidal height. According to (2), the maximum flow velocity over the sill is about 90 cm s^{-1} during spring tides and about 30 cm s^{-1} during neap tides. During 1982, CTD stations were taken at two to three month intervals along the axis of the inlet system (Fig. 1), and estimates of the phase speed c_i in (1) were made from these collected density profiles. By taking the sill crest to be at a depth of 60 m and using density data collected during the second week of June, the mode one phase speed over the sill is calculated to

have been 120 ± 10 cm s^{-1}. This result comes from three separate estimates of c_i that were calculated from the density profiles collected from the three CTD stations closest to the sill (Fig. 4). Since the sectionally averaged tidal velocity over the sill crest during spring tides is about 90 cm s^{-1}, it can be seen from (1) that the flow over the sill was at all times subcritical to the mode one response. Although the Froude number has been crudely defined and can only be used as an indication of what the flow conditions were like, this suggests that the hydraulic jump was not primarily a mode one response except possibly near maximum tidal velocity. Farmer and Denton (1985) consider the flow in Figure 5c, which is near maximum tidal velocity, to be critical with respect to the first mode. The mode two phase speed over the sill on the other hand was 35 ± 1 cm s^{-1}, which is significantly less than the maximum tidal velocity at the sill crest during spring tides. Therefore, for a substantial portion of each tidal cycle during spring tides, the mode two response likely could have been a hydraulic jump. This observation has influenced our analysis of the flow, as will be seen later.

3. The equations

Since the flow is very complex our concentration has been focused on a particular process, namely the hydraulic transitions in the lee of the sill. One way to analyze these transitions is with the nonlinear, shallow water equations. When using the shallow water equations the water column is approximated as a number of uniform layers of different density. For an N-layer flow in which there are no cross-channel variations we have, for $1 \leqslant i \leqslant N$

$$\frac{\partial u_i}{\partial t} + \frac{\partial}{\partial x}\left(\frac{u_i^2}{2}\right) = -\frac{1}{\rho_0}\frac{\partial p_s}{\partial x} - \sum_{j=0}^{i-1}\left[\frac{g\rho_j'}{\rho_0}\frac{\partial}{\partial x}\left(\sum_{k=j+1}^{N+1} h_k\right)\right] - \frac{C_D}{h_i}\sum_{\substack{j=i-1 \\ 1\leqslant j\leqslant N}}^{i+1}[(u_i - u_j)|u_i - u_j|] \quad (3)$$

$$\frac{\partial h_i}{\partial t} + \frac{\partial}{\partial x}(u_i h_i) = 0 \quad (4)$$

where u_i and h_i ($1 \leqslant i \leqslant N$) are the velocity and thickness of the ith layer, h_{N+1} the height of the bottom boundary above a reference level, p_s the surface pressure, g the acceleration due to gravity, $\rho_0' = 0$, ρ_i' ($1 \leqslant i \leqslant N-1$) the density change across the ith interface, ρ_0 a water density representative of the entire water column ($\approx 10^3$ kg m^{-3}), and C_D a dimensionless drag coefficient (Fig. 7). The interfacial stress terms have been included in the momentum equations in order to allow for the vertical transport of momentum by shear stresses within the body of the fluid. (They turned out to be unimportant, but there was no way of knowing this ahead of time.) The drag coefficient was set equal to 0.003, a value consistent with those used for the drag against solid boundaries.

By restricting the model to two dimensions, we are forced to ignore both cross channel variations in the sill depth and Coriolis forces. There are in fact significant variations in the sill depth (Fig. 2a), but it is beyond the scope of this paper to include these variations. Relative to the first mode internal wave, the Rossby radius of deformation is about 10 km, which is much greater than the width of the inlet. Relative to the second mode (we examine a three-layer flow in section 4) the Rossby radius is about 4 km, so Coriolis forces could influence the large scale mode two response. They probably have only a minor influence on the nonlinear processes occurring downstream of the sill, however. A particle of water traveling at 50 cm s^{-1} would take less than ten minutes to move the distance from the sill crest to the trough in the streamlines of Fig. 5 ($\approx$100 m). This time interval is much shorter than the rotation period of the earth.

Another simplification is made by approximating the surface of the inlet as a motionless rigid lid. This should have little effect on the model results because 1) the changes in tidal height only cause about a 10% variation in the total depth over the sill crest, and 2) the phase of the barotropic tide only varies by a few degrees along the inlet. When this simplification is made, the surface pressure p_s in (3) becomes the pressure along the rigid lid.

The maximum depth in the modeled flow has been limited to 125 m, a depth we feel is representative of the upstream blocking depth and downstream boundary layer separation depth of the flows in Figs. 5a and 5b. There is obviously considerable uncertainty in this value, but for our purposes we feel we do not need to determine it precisely. The streamlines in Figs. 5a and 5b, which were observed over one of the shallowest regions of the sill, indicate downstream flow separation at a depth of about 100 m. (Note the dark band of scatterers at that depth.) This observation is consistent with the experimental results of Huppert and Britter (1982), which found the point of separation to occur directly beneath hydraulic jumps. Separation appears to occur near the sill crest in the anomalous flow (Fig. 5b) and we will not attempt to model it in this paper. The blocking depth is much harder to determine, but we estimate from the velocity profiles in Figs. 6a and 6b that it cannot be shallower than about 60 m. In general, both the blocking and separation depths are functions of the tidal forcing, but no attempt will be made here to simulate this time dependent property of the flow. A schematic of the modeled flow is shown in Fig. 7.

Some manipulation can change (3) and (4) into a form more suitable for solution. From (4) we obtain

$$\frac{\partial H}{\partial t} + \frac{\partial}{\partial x}\left(\sum_{i=1}^{N} M_i\right) = 0 \quad (5)$$

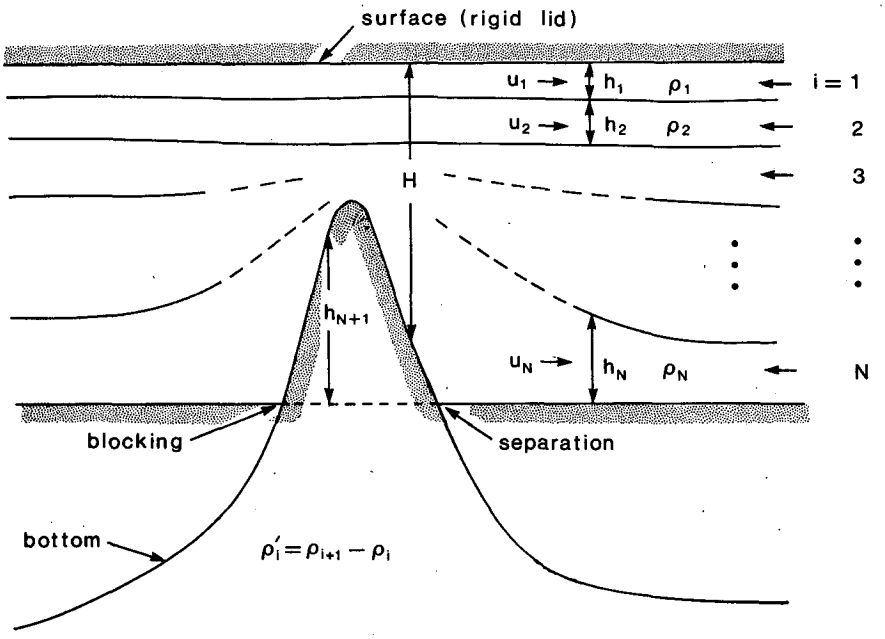

FIG. 7. Diagram of an N-layer flow. The maximum depth in the model is the depth of upstream blocking and flow separation, and the top of the upper layer in the model is a rigid lid.

where $M_i = u_i h_i$ and

$$H = \sum_{i=1}^{N} h_i. \tag{6}$$

Since H is not a function of time, (5) can be integrated to obtain

$$\sum_{i=1}^{N} M_i = F(t) \tag{7}$$

where $F(t)$, the total volume transport at any position along the inlet, is a prescribed function. We see from (6) and (7) that if the volume transport and thickness of $N-1$ layers are known, then the volume transport and thickness of the remaining layer are also known. In this paper the flow in the lower layers has been determined from the differential equations, and the flow in the surface layer determined from the constraints that the total water depth and total volume transport are known. Also, instead of solving for the velocity and thickness of the layers, the volume transport and thickness have been calculated. Substituting (4) into (3) one obtains

$$\frac{\partial M_i}{\partial t} + \frac{\partial}{\partial x}\left(\frac{M_i^2}{h_i}\right) = \frac{-h_i}{\rho_0}\frac{\partial p_s}{\partial x} - h_i \sum_{j=0}^{i-1}\left[\frac{g\rho_j'}{\rho_0}\frac{\partial}{\partial x}\left(\sum_{k=j+1}^{N+1} h_k\right)\right] - C_D \sum_{\substack{j=i-1 \\ 1\leqslant j\leqslant N}}^{i+1} [(u_i - u_j)|u_i - u_j|]. \tag{8}$$

Using (6) and (7), and the equation for M_1 to eliminate the surface pressure, we obtain, for $2 \leqslant i \leqslant N$,

$$\frac{\partial M_i}{\partial t} = \frac{-\partial}{\partial x}\left(\frac{M_i^2}{h_i}\right) - h_i \sum_{j=0}^{i-1}\left[\frac{g\rho_j'}{\rho_0}\frac{\partial}{\partial x}\left(\sum_{k=j+1}^{N+1} h_k\right)\right] - C_D \sum_{\substack{j=i-1 \\ 1\leqslant j\leqslant N}}^{i+1} [(u_i - u_j)|u_i - u_j|] + \frac{h_i}{H}\left\langle \sum_{l=1}^{N}\left\{h_l \sum_{j=0}^{l-1}\left[\frac{g\rho_j'}{\rho_0}\frac{\partial}{\partial x}\left(\sum_{k=j+1}^{N+1} h_k\right)\right] + \frac{\partial}{\partial x}\left(\frac{M_l^2}{h_l}\right)\right\} + \frac{dF}{dt}\right\rangle \tag{9}$$

which can be solved together with the continuity equations

$$\frac{\partial h_i}{\partial t} + \frac{\partial M_i}{\partial x} = 0. \tag{10}$$

The momentum and continuity equations, (9) and (10), are now in the form in which they were solved, except for diffusion terms that were added to help maintain the stability of the solutions. These terms are of a type given in Richtmyer and Morton (1967), and are described in detail at the end of this section.

The barotropic forcing enters the problem via the boundary conditions and the total volume transport $F(t)$, the derivative of which appears as a forcing term in (9). Since we are interested in the baroclinic response to tidal forcing, $F(t)$ is given a sinusoidal dependence on time and is expressed as

$$F(t) = F_0 \sin(\omega t) \tag{11}$$

where F_0 is a constant indicative of the strength of the tide and ω the angular frequency of the tide. The boundary conditions (at $x = -L$ and L) are specified far from the sill so that any influence the boundaries have on the flow will not have propagated into the region of the sill before the numerical calculation is over. They are given by

$$\left.\begin{aligned} h_i(-L, t) &= h_i(-L, 0) \\ h_i(L, t) &= h_i(L, 0) \\ M_i(-L, t) &= F(t)\frac{h_i(-L, t)}{H(-L)} \\ M_i(L, t) &= F(t)\frac{h_i(L, t)}{H(L)} \end{aligned}\right\}, \quad 2 \leqslant i \leqslant N. \tag{12}$$

The two-step version of the Lax-Wendroff integration scheme (e.g., see Richtmyer and Morton, 1967) was used to solve (9) and (10), after first adding diffusion terms so that the solutions would remain stable. It is a numerical scheme commonly used when solving problems of the type being presented here. For example, versions of this scheme were used by Houghton and Kasahara (1968) and Houghton and Isaacson (1970). In cases where interfacial shear stresses have not been included in the equations, i.e., when $C_D = 0$, it has been found that an artificial viscosity must at times be added to the equations before stable solutions are obtained (Richtmyer and Morton, 1967; Houghton and Isaacson, 1970). In the present case the interfacial drag has a stabilizing influence on the solutions, but artificial viscosities were still required to aid in smoothing out small wavenumber oscillations in the region of the sill. Diffusion terms of the form

$$\left.\begin{aligned} \frac{\partial}{\partial x}\left((a\Delta x)^2\left|\frac{\partial u_i}{\partial x}\right|\frac{\partial h_i}{\partial x}\right) &= \frac{\partial E_i}{\partial x} \\ \frac{\partial}{\partial x}\left((a\Delta x)^2\left|\frac{\partial u_i}{\partial x}\right|\frac{\partial M_i}{\partial x}\right) &= \frac{\partial D_i}{\partial x} \end{aligned}\right\}, \quad 1 \leqslant i \leqslant N \tag{13}$$

were added to the rhs of (4) [also (10)] and (8) respectively, where a is a dimensionless constant (set equal to 0.5) and Δx is the distance between the grid points of the numerical model. These terms are very similar to those described by Richtmyer and Morton in connection with the Lax-Wendroff integration scheme. It is important to note that the value for a has also been taken from Richtmyer and Morton. It has not been adjusted so that the model results (section 4) would agree as closely as possible with the observations presented in section 2.

Since the terms (13) are very small, except in the region of the hydraulic jump and where high wavenumber oscillations develop, they were simplified in order to make the calculations easier. Assuming the derivatives of E_i with respect to time are small, (9) is modified by the diffusion terms added to (4) and (8) to take the form

$$\frac{\partial M_i}{\partial t} = \cdots + \frac{\partial D_i}{\partial x} - \frac{h_i}{H}\frac{\partial}{\partial x}\left[\sum_{j=1}^{N} D_j\right]. \tag{14}$$

The constraint (7) becomes

$$\sum_{i=1}^{N} (M_i - E_i) = F(t). \tag{15}$$

It is much more difficult to calculate M_1 from (15) than from (7) because (15) contains within it the term $|\partial u_1/\partial x|$. Therefore, the approximation

$$\left|\frac{\partial u_1}{\partial x}\right| \approx \left|\frac{\partial}{\partial x}\left(\frac{F(t) - \sum_{i=2}^{N} M_i}{h_1}\right)\right| \tag{16}$$

has been used so that

$$M_1 = u_1 h_1 \approx F(t) - \sum_{i=2}^{N} (M_i - E_i) + (a\Delta x)^2\left|\frac{\partial}{\partial x}\left(\frac{F(t) - \sum_{i=2}^{N} M_i}{h_1}\right)\right|\frac{\partial h_1}{\partial x}. \tag{17}$$

The differenced equations are listed in the Appendix. The distance between grid points was set at 10 m and a time step at 2 s was used to give the results shown in the next section.

For the purposes of modeling the flow over the sill of Observatory Inlet, it is necessary to divide the water column into at least three layers. If the water column is divided into only two layers, there can be only the mode one response which, even during spring tides, remains subcritical over the entire tidal cycle (section 2). When a third layer is added, one obtains the mode two response that is supercritical over the sill crest for a substantial portion of each tidal cycle during spring tides. Therefore, a three-layer flow is the simplest model capable of producing the observed hydraulic transitions.

4. Comparison with data

a. Before maximum tidal velocity

First, we consider the streamlines in Fig. 5a (also shown in Fig. 8a) and the corresponding velocity profiles in Fig. 6a.

The acoustic measurements of water velocity are that component of the total velocity parallel to the axis of the acoustic beam. To compare these observations to the layered numerical model, the measurements were put into a more practical form by assuming that the

total velocity U_T was everywhere horizontal and parallel to the axis of the inlet system. Then

$$U_T = \frac{U_M}{\cos\theta}$$

where U_M is the velocity measured along the beam and θ the angle of the beam to the horizontal. There is of course some error involved in making this transformation because the flow obviously will not always satisfy the assumptions. The magnitude of the error certainly varies with position and is hard to estimate. It is likely reduced, however, by using averaged values of U_T. This was done by dividing the water column below the surface layer into two layers, thus making three layers in total, and then calculating the average value of U_T in the lower two layers. Recall that the velocity in the surface layer could not be measured by the Doppler probe (section 2). The division was done arbitrarily by picking a particular streamline to be the boundary between the layers. For the flow in Fig. 5a, a streamline passing about 15 m above the sill crest was chosen. It is a level where reflectors are concentrated and also forms a lower envelope of the trough downstream of the sill. The averaged velocities for the layers (and the model results, which are described later) are plotted in Fig. 8b.

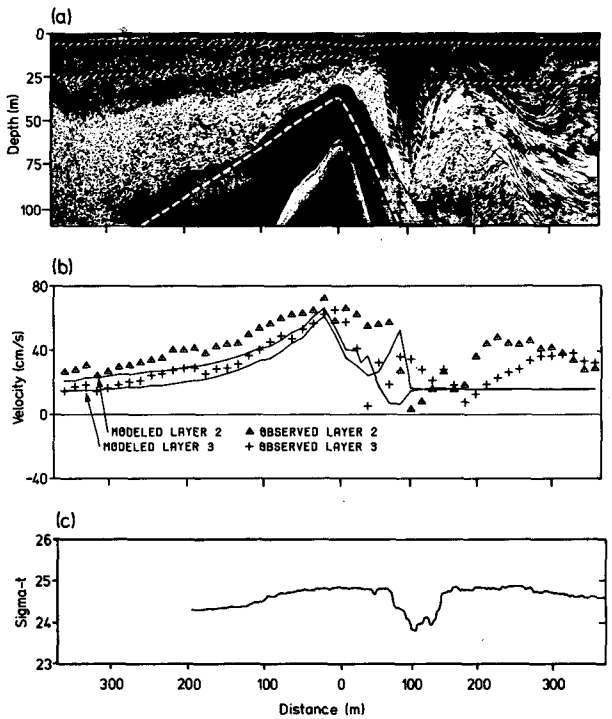

FIG. 8. (a) Predicted interface positions for a three-layer flow plotted over the observed streamlines (also shown in Fig. 5a). One dashed line indicates the bottom profile used in the numerical model, and the other two indicate the predicted interface positions. (b) Predicted and observed velocities in the lower two layers. The forcing in the model was adjusted to make the predictions and observations agree at the sill crest. In order to compare the acoustically measured velocities with the model predictions, it has been assumed here that the observed flow is everywhere horizontal. (c) Sigma-t trace obtained by drifting a CTD across the sill crest at a depth of approximately 25 m.

Upstream of the sill, the velocity in both layers increases towards the sill crest with the velocity in the middle layer being systematically larger than that in the lower. The velocity measurements in the lower layer downstream of the sill crest exhibit more scatter than those in the upper layer, and they may indeed be more variable because of the influence of localized variations in the bottom topography. However, the scatter is also due at least in part to contamination of the acoustical signal by reflections off the bottom of the inlet (Zedel, 1985). At the sill crest the velocities in each layer are comparable at about 60 cm s^{-1}. Since the measurements were made 2.8 hours into the tide, this velocity is approximately the maximum value. It is significantly less than the 90 cm s^{-1} calculated from measurements of the tidal height and suggests that water is being preferentially directed to deeper parts of the inlet in a manner analogous to the flow around mountains. The sill depth was about 30 m where the measurements were made (Fig. 8a) whereas parts of the sill are as much as 60 m in depth (Fig. 2a). The flow velocity was probably greater over the deeper parts of the sill. The significance of this will be discussed at the end of this section, after first developing the model to reproduce the observed velocities and streamlines.

The acoustic observations indicate a sill depth of about 30 m; however, the sill profile used in the model and shown in Fig. 8a has a minimum depth of 40 m. Since there is substantial cross-channel variation in the topography this difference between the model topography and that observed acoustically is felt to be acceptably small. In fact, it will be shown later that a sill depth of 50 m is probably the most appropriate for modeling the streamlines.

The velocity in the model was initially set equal to zero. The forcing was adjusted so that the predicted velocity over the sill crest would, at the proper time during the tidal cycle, be the same as the observed velocity. This meant setting F_0 in (11) equal to 20 m^2 s^{-1}. The angular frequency in (11) was set equal to 1.405×10^{-4} s^{-1}, the value for the M_2 tide (T = 12.42 h). The surface layer was given an initial depth of 10 m and a density change across its interface of 20 kg m^{-3}. This is consistent with the observed profile (Fig. 4). The interface separating the lower two layers was chosen to correspond to the streamline used in calculating the velocities in Fig. 8b. Because the interface rises with time over the sill crest as the tidal velocity increases, the interface was given an initial depth only 5 m shallower than the modeled sill crest. The density difference across the lower interface was adjusted to make the predicted streamline match the observed streamline. It turned out that a density difference of 0.2 kg m^{-3} produced quite good results. The suitability

of this choice for the density difference will be discussed in more detail at the end of this section when the influence on the flow of cross-channel variations in the inlet is examined.

The theoretical interface positions corresponding to the flow in Fig. 8a have been drawn in and we see that they compare favorably to the observations. The large trough in the immediate lee of the sill is well simulated. The lee waves downstream of the trough are not reproduced because the model is hydrostatic. Note in particular that the lower interface of the model deepens suddenly about 60 m downstream of the sill crest. This sudden deepening is also evident in the observations.

The theoretical velocities in the bottom two layers have been plotted over the data in Fig. 8b. In accord with the observations, upstream of the sill crest the theoretical velocity is greater in the middle layer than in the lower. As the flow approaches the sill, the interface separating the bottom two layers rises, and this causes the velocity in the middle (lower) layer to increase (decrease). The good agreement indicated in this part of the flow suggests that flow velocity upstream of the sill crest did not have a strong cross-channel component. Any redirection of water to deeper parts of the inlet must have occurred primarily outside the region spanned by the observations.

Downstream of the sill crest the agreement between the modeled velocities and the observations is not as good. Immediately downstream of the sill crest, just preceding the trough, the observed middle layer velocities are appreciably higher than the model velocities as a result of the strong downward flow occurring there. That is, the assumption of horizontal flow that was used to convert the velocity observations fails in this region. The streamlines suggest that the flow is downward at approximately 60° to horizonal. Based on the Doppler speed measurement of 25 cm s^{-1} along the acoustic beam axis, the net horizontal velocity is actually ~ 13 cm s^{-1}. This estimate cannot be considered accurate but it does indicate that the reduced model velocities of this region are reasonable.

The peak in the theoretical velocity below the trough is not readily discernable in the observed velocities because of the scatter in the observations. Also, as expected, the theory begins to diverge noticeably from the observations once the lee waves downstream of the trough are encountered.

Considering the number of assumptions that have been made, we feel the model is adequately simulating the observed flow before maximum tidal velocity. Still, it must be remembered that the density difference across the lower interface has been used as a free parameter, and that the measured velocity at the sill crest is less than that calculated from measurements of the tidal height. This problem will be addressed after first examining how the modeled flow evolves with time, to see if it can simulate the observed transition in the flow after maximum tidal velocity.

b. The evolution of the flow with time

In Fig. 9 the theoretical interfaces and velocities at different times during the tide are plotted in order to show how the flow evolves with time. We see that the flow is qualitatively the same before and after maximum tidal velocity (Fig. 9c, d). Contrary to the observations, the predicted streamlines do not change dramatically as soon as the flow rate begins decreasing. Instead, for most of the tide they remain similar to the observed flow in Fig. 8a with the streamline which separates the bottom two layers extending almost horizontally beyond the sill crest before plunging steeply downwards. It is only just before slack tide that the trough in the lee of the sill migrates upstream (Fig. 9f).

It is possible that the transition observed in the flow at maximum tidal velocity was caused by the temporal variability of processes not accounted for in the model. For example, it may be that the rate of change in the level of flow separation and nonhydrostatic effects had an important influence on the hydraulic response near the sill crest. Also, note that the predicted velocity in the surface layer is relatively insensitive to variations in the bottom topography, and therefore that the velocity shear between the surface and middle layers can be substantial immediately upstream of the sill crest. This means that during the tidal cycle vertical mixing may have significantly altered the density structure over the sill crest, and consequently altered the dynamics of the flow. In addition, once the tide began decelerating, horizontal pressure gradients caused by intense downstream mixing may have forced the streamlines closer to the sill crest. They may even have induced reversals in the flow direction, and thereby caused substantial modification of the streamlines. The streamlines appear to lose their integrity downstream of the sill after maximum tidal velocity (Fig. 5b), so perhaps a layered interpretation of the flow becomes inappropriate.

As an aside, it is interesting to note that near slack tide (Fig. 9f, l) the height of the lower interface and the velocity in the middle layer are greater upstream of the sill than downstream. As the tidal forcing goes to zero and then reverses, this inequality in height and velocity also reverses, and an internal wave is generated. This wave is beyond the scope of this paper and will not be discussed further.

c. Modification of the model's parameters

The value used for the density difference across the lower interface will now be examined. Recall that the streamlines in Fig. 8 are well predicted as long as the density difference across the lower interface is set equal to 0.2 kg m^{-3}. Observations of the density, however, make this value hard to support. Figure 8c shows a density trace that was made by drifting a CTD at constant depth across the sill. We see that the density

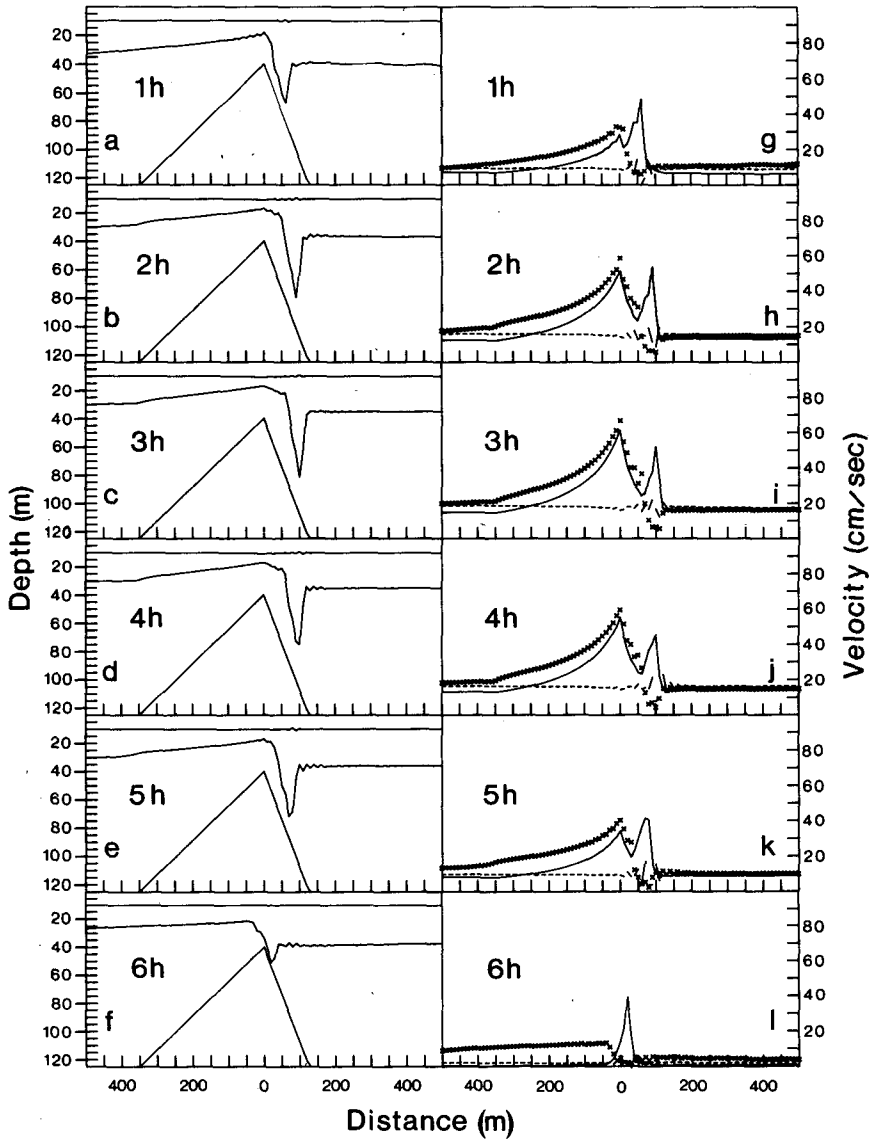

FIG. 9. Theoretical interface positions and velocities at hourly intervals during the ebb tide when the tidal period is 12.42 h. The velocity in the bottom layer is given by the solid line, the velocity in the middle layer is given by the crosses, and the velocity in the surface layer is given by the dashed line.

changed by about 1 kg m^{-3} across the trough, which is a value five times greater than that used in the model. This large discrepancy can be reconciled by considering both the forcing that was used in the model and the Froude number of the flow.

Recall that the forcing was adjusted to give the observed velocity at the sill crest, and that this velocity is less than the maximum velocity of 90 cm s^{-1} calculated from the observations of the tidal height. Taking 50 m to be a depth representative of the sill crest as a whole, the forcing required to give a maximum sectionally averaged velocity of 90 cm s^{-1} can be determined from (11). One obtains

$$F_0 = (0.9 \text{ m s}^{-1})(50 \text{ m})$$
$$= 45 \text{ m}^2 \text{ s}^{-1}$$

which is 2.25 or $\sqrt{5}$ times greater than the forcing of 20 m^2 s^{-1} actually used. This means that the barotropic velocity on both sides of the sill would be increased by a factor of 2.25 if F_0 were increased to 45 m^2 s^{-1}.

The mode-2 Froude number is

$$F_2 \approx \frac{U}{c_2} \tag{18}$$

where U is the barotropic velocity and c_2 is the mode-

2 phase speed according to linear theory. For a three-layer fluid we find from (3) and (4) that

$$c_2^2 = \frac{g\rho_1' h_1(h_2 + h_3) + g\rho_2' h_3(h_1 + h_2)}{2H} - \left[\left(\frac{g\rho_1' h_1(h_2 + h_3) - g\rho_2' h_3(h_1 + h_2)}{2H}\right)^2 + \left(\frac{gh_1h_3}{H}\right)^2 \rho_1'\rho_2'\right]^{1/2} \quad (19)$$

which, for the layer thicknesses being used here, reduces to

$$c_2 \approx \left[\frac{g\rho_2' h_2 h_3}{h_2 + h_3}\right]^{1/2} \quad (20)$$

when $\rho_1' \gg \rho_2'$. Note that when $\rho_2' = 1$ kg m^{-3} and the bottom is set at a depth of 60 m, i.e., $h_2 = h_3 = 25$ m, one obtains from (20) that $c_2 = 35$ cm s^{-1}, which is equal to the average value calculated for c_2 from the measured density profiles (section 2). Therefore, when $\rho_2' = 1$ kg m^{-3} the model flow and the actual flow should have similar mode two responses near the sill crest. Also, we see from (18) and (20) that increasing the density difference by a factor of five and increasing the volume flux by a factor of $\sqrt{5}$ leaves the mode-2 Froude number on either side of the sill unchanged. This implies that the shape of the lower interface should also be unchanged. In Fig. 10a the theoretical streamlines for this new flow are plotted over the observations. The topography in the model has been changed only in that the sill is not allowed to become shallower than 50 m. We see that, as long as the imposed forcing is representative of the sectionally averaged velocity, the theoretical streamlines correspond closely to the observations when the measured density difference is used. By adjusting the topography in the lee of the sill and the depth of flow separation, the predicted streamlines can be brought into even closer agreement with the observations. However, these cosmetic changes are hardly warranted, since there is substantial cross-channel variability in the topography. The results presented here imply that the streamlines are being influenced more by the sectionally averaged velocity than by the local value. That is, the streamlines appear to be weak functions of the cross-channel position even though the velocities may vary substantially. It is reasonable to expect therefore that the observed streamlines are representative of what the flow was like over much of the width of the sill.

Figure 10b shows the velocities corresponding to the theoretical streamlines in Fig. 10a. They may be more representative of the flow as a whole than the measured velocities. Although they are qualitatively similar to the corresponding velocities shown in Fig. 8b, they are larger because of the increased forcing. Note that even though the maximum barotropic velocity over the sill

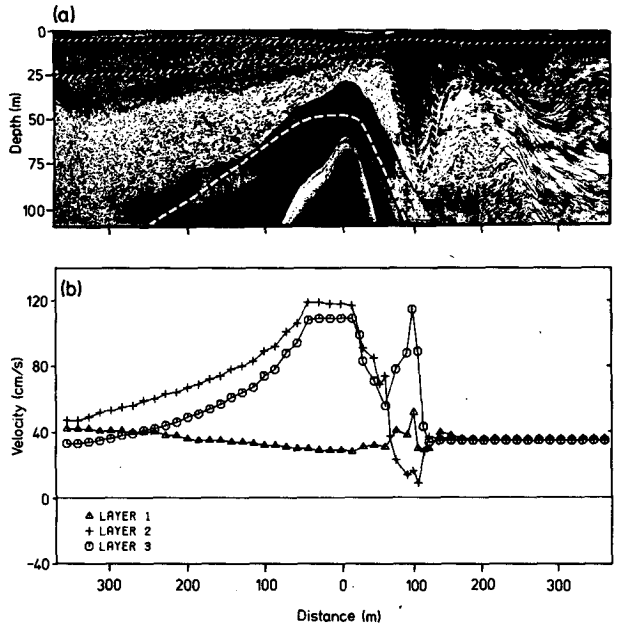

FIG. 10. Theoretical interface positions (a) and velocities (b) when the sill depth is set equal to 50 m, the forcing is increased to give the calculated barotropic velocity over the sill crest, and the density difference across the lower interface is set equal to a value consistent with the sigma-t trace in Fig. 8c. One dashed line in (a) indicates the bottom profile used in the numerical model, and the other two indicate the predicted interface positions.

crest is 90 cm s^{-1}, speeds in excess of 100 cm s^{-1} are produced because of the baroclinicity of the flow.

5. Dissipation

We want to estimate the energy dissipated by the hydraulic flow so that we can compare it to the total amount of energy removed from the barotropic tide. Stacey (1984) shows that, averaged over a spring-neap cycle, energy was removed from the barotropic tide during June 1982 at a rate of approximately 25 megawatts.

In the model presented here, both the exchange of momentum between the layers and the diffusion of momentum within each layer cause energy to be dissipated. The terms representing this dissipation can be calculated from (8) and (10) with the diffusion terms (13) included. They are

$$\left.\begin{aligned} P_1 &= W\int_{-\infty}^{+\infty}\left[\sum_{i=1}^{N-1}\rho C_D|\Delta u_i|(\Delta u_i)^2\right]dx \\ P_2 &= W\int_{-\infty}^{+\infty}\left[\sum_{i=1}^{N}\rho A_i h_i\left(\frac{\partial u_i}{\partial x}\right)^2\right]dx \end{aligned}\right\} \quad (21)$$

where W is the width of the inlet near the sill ($\leq$2.5 km), N the number of layers, Δu_i the velocity difference

across the ith interface and A_i the eddy viscosity in the ith layer. In the model being used here

$$A_i = (a\Delta x)^2 \left|\frac{\partial u_i}{\partial x}\right| . \tag{22}$$

Only the dissipation up until maximum tidal velocity will be calculated because that is when the model simulates the flow the most accurately. After maximum tide, mixing that the model cannot take into account is probably responsible for a significant amount of the dissipation. However, it is unlikely that the energy utilized by the flow after maximum tidal velocity was an order of magnitude greater than the amount utilized before. It is also unlikely that an order of magnitude more energy was dissipated while the tide was flowing in the opposite direction, since the topography on either side of the sill is not dramatically different.

Averaged over the quarter of a tidal cycle of interest, the rate at which energy is dissipated is

$$P_{\text{av}} = \frac{4}{T}\int_0^{T/4} (P_1 + P_2)dt. \tag{23}$$

Since the model is simulating a flow observed during a spring tide, P_{av} is the dissipation averaged over one quarter of a semidiurnal tidal cycle during a spring tide. In Observatory Inlet, the dissipation averaged over a semidiurnal tidal cycle during neap tides is much less than this, because then the tidal currents are less by a factor of three and dissipation depends roughly on the cube of the velocity. Averaged over a spring-neap tide, therefore, the rate at which energy is dissipated is

$$\bar{P} \approx \frac{P_{\text{av}}}{2} . \tag{24}$$

The average dissipation P_{av} was calculated using a sill depth of 50 m, a maximum barotropic velocity over the sill crest of 90 cm s^{-1}, and a density difference across the lower interface of 1 kg m^{-3}. Recall that these parameters produced the flow in Fig. 10. One obtains $P_{\text{av}} \approx 3$ megawatts or $\bar{P} \approx 1.5$ megawatts, which is only 6% of the total power removed from the tide. Also, $P_1/P_2 \approx 0.14$, so the interfacial shear stresses were relatively unimportant and need not have been included. Almost all of the dissipation is due to P_2, and, as expected, almost all of this occurs in the immediate vicinity of the hydraulic transition in the lee of the sill. According to this calculation, the hydraulic flow utilized only a small percentage of all the energy removed from the tide.

From this calculation of the dissipation, total drag coefficients can be determined. One has

$$C_T(t) = \frac{D}{\frac{1}{2}\rho U^2 h_s} = \frac{P_1 + P_2}{\frac{1}{2}\rho U^3 h_s} \tag{25}$$

where D is the total drag on the sill, U the barotropic velocity far from the sill and h_s the height of the sill (e.g., see Turner, 1973). Here, h_s is taken to be the height of the sill above the level of upstream blocking and flow separation. The total drag coefficient $C_T(t)$ changes as the tidal forcing changes. In Fig. 11, C_T has been plotted against F_2^{-1} [see (18)] for various tidal exchange rates over the measurements of Davis (1969). Davis measured the drag on a thin obstacle in a linearly stratified fluid, i.e., N = Brunt-Väisälä frequency = constant, and determined the drag coefficient as a function of $k = Nh_s/\pi U$, which is like an inverse Froude number. We see that the drag coefficients calculated from the model are similar to those measured by Davis. There is, of course, no reason to expect them to correspond exactly, since the stratification and topography are not the same in the two cases, and the model does not take into account all of the nonlinear processes that can occur in the vicinity of a sill. Nonetheless, the fact that they are of the same order of magnitude is encouraging.

It is realized that this numerical calculation of the dissipation must be treated with caution. However, it is felt to be accurate to within an order of magnitude because 1) the model, when using a reasonable forcing function and density structure, adequately describes the observed flow up until maximum tidal velocity even though the parameter a in (22) was not adjusted to tune the model, and 2) as just described, values calculated from the model for the total drag coefficient are of the same order of magnitude as those measured by Davis (1969). The implication is that, although the hydraulic flow is certainly very important in the vicinity of the sill, it probably does not directly make a significant contribution to the energy budget of the inlet as a whole.

As a check on the above calculation, one can estimate the dissipation across the hydraulic jump by determining the energy flux (both kinetic and potential) on either side of the jump. In a steady state flow, the difference in energy flux across the jump is equal to

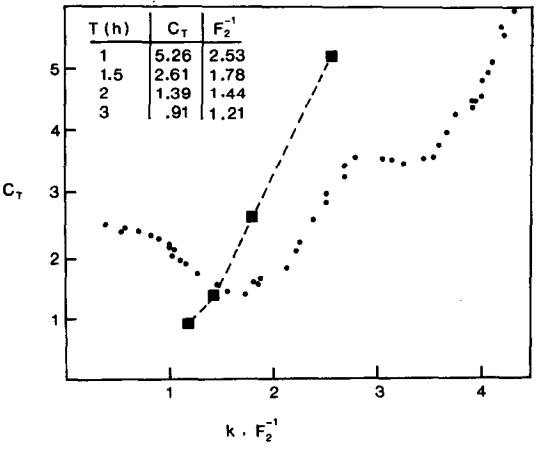

FIG. 11. Theoretical drag coefficients plotted over the data of Davis (1969).

the rate at which the jump is dissipating energy. Therefore, to check the dissipation calculation, the energy flux (the kinetic energy flux in the lowest two layers and the potential energy flux due to the lower interface) towards the sill 500 m upstream of the sill crest, and away from the sill 500 m downstream of the sill crest was calculated as a function of time. The average change in energy flux across the jump could then be determined. This gives the dissipation due to the drag coefficient, eddy viscosity and numerical scheme, i.e., the numerical dissipation, and, because the flow is time dependent, includes an amount of energy that will not be dissipated locally but rather will eventually be transported away from the sill as part of the internal tide. The calculation therefore has the advantage of taking into account numerical dissipation, but the disadvantage of being an overestimate. It does however put an upper bound on the dissipation. It is calculated, remembering to divide by 2 [see (24)], that energy accumulated in the region of the sill at a rate of 2.3 megawatts, which is still only 9% of the total power withdrawn from the barotropic tide.

6. Conclusions

The nonlinear flow over the sill of Observatory Inlet has been examined using a time dependent, hydraulic model. In particular, the flow of a spring tide during the summer of 1982 has been analyzed. During the time of the observations there was substantial freshwater runoff, and so the inlet had a distinct surface layer.

When the tide is accelerating, a three-layer hydrostatic model adequately simulates the flow. The streamlines extending almost horizontally beyond the sill crest and the hydraulic jump which follows downstream are well simulated. The lee waves downstream of the hydraulic jump are not reproduced because the model is hydrostatic. Differences between the acoustically measured velocities and those calculated from measurements of the tidal height suggest that the current velocity was sensitive to cross-channel variations in the bottom topography, i.e., water was preferentially directed to deeper parts of the sill in a manner analogous to the flow around mountains. The model's successful simulation of the streamlines in spite of this suggests that the streamlines were not greatly influenced by the cross-channel topographic variations in the inlet.

When the tide began decelerating the observed flow underwent a transition that the three-layer model does not predict. Since the model is time dependent, its failure to predict this transition suggests that the change was not caused solely by the rate at which the tidal forcing was varying.

It is estimated that the hydraulic flow utilized only about 5% of all the energy removed from the barotropic tide. Although this result is probably accurate only to within an order of magnitude, it suggests, in agreement with Stacey (1984), that processes other than those studied in this paper are withdrawing most of the energy from the barotropic tide.

Acknowledgments. The authors wish to thank D. M. Farmer for many stimulating discussions and helpful suggestions. The cooperation and assistance of the Ocean Physics Section at the Institute of Ocean Sciences is also very much appreciated. The observations presented in this paper were made by L. Zedel and Dr. Farmer as part of L. Zedel's University of Victoria M.Sc. project. While pursuing this work M. Stacey was supported as a visiting Fellow by the Canadian Government and L. Zedel received funding through a Science Council of British Columbia G.R.E.A.T. award.

APPENDIX

The Two-Step Integration Scheme Used to Solve the Shallow Water Equations

Definitions

Let B^n_{ip} be a property of the ith layer at time $n\Delta t$ and position $p\Delta x$, where p and n are integers.

Then
$$\langle B^n_{ip} \rangle = \frac{B^n_{i(p+1)} + B^n_{ip}}{2}$$

$$\delta_x(B^n_{ip}) = \frac{B^n_{i(p+1)} - B^n_{ip}}{\Delta x}$$

First Time Step: Calculation of intermediate values of M_i and h_i.

Let $F^n = A \sin(\omega \Delta t n)$

$$\frac{dF^n}{dt} = \omega A \cos(\omega \Delta t n)$$

$$H_p = \sum_{i=1}^{N} h^n_{ip}, \quad \text{which is independent of } t \text{ and is known}$$

$$M^n_{1p} = F^n - \sum_{i=2}^{N} M^n_{ip}$$

$$h^n_{1p} = H_p - \sum_{i=2}^{N} h^n_{ip}$$

$$u^n_{ip} = \frac{M^n_{ip}}{h^n_{ip}}$$

$$J^n_{ip} = \frac{(M^n_{ip})^2}{h^n_{ip}}$$

$$R^n_{jp} = \sum_{k=j+1}^{N+1} h^n_{kp}.$$

Then the intermediate values of M_i and h_i $(2 \leqslant i \leqslant N)$ are

$$\bar{M}^{(n+1)}_{i(p+1)} = \langle M^n_{ip} \rangle - \frac{\Delta t}{2}\left\{\delta_x(J^n_{ip}) + \langle h^n_{ip}\rangle \times \sum_{j=0}^{i-1}\left(\frac{g\rho'_j}{\rho_0}\,\delta_x(R^n_{jp})\right) + C_D \times \sum_{\substack{j=i-1\\ 1\leqslant j\leqslant N}}^{i+1} \langle u^n_{ip} - u^n_{jp}\rangle\langle|u^n_{ip} - u^n_{jp}|\rangle\right\} + \frac{\Delta t}{2}\left\{\frac{\langle h^n_{ip}\rangle}{\langle H_p\rangle} \times \sum_{l=1}^{N}\left[\langle h^n_{lp}\rangle \sum_{j=0}^{l-1}\left(\frac{g\rho'_j}{\rho_0}\,\delta_x(R^n_{jp})\right) + \delta_x(J^n_{lp})\right] + \frac{dF^n}{dt}\right\}, \tag{A1}$$

$$\bar{h}^{(n+1)}_{i(p+1)} = \langle h^n_{ip}\rangle - \frac{\Delta t}{2}\,\delta_x(M^n_{ip}). \tag{A2}$$

Second Time Step: Calculation of new values of M_i and h_i.

Let
$$D^n_{ip} = a^2|u^n_{ip} - u^n_{i(p-1)}|(M^n_{ip} - M^n_{i(p-1)})$$
$$E^n_{ip} = a^2|u^n_{ip} - u^n_{i(p-1)}|(h^n_{ip} - h^n_{i(p-1)})$$
$$\bar{M}^n_{lp} = F^{(n+\frac{1}{2})} - \sum_{i=2}^{N}\bar{M}^n_{ip} + \sum_{i=1}^{N} E^n_{ip}$$
$$\bar{h}^n_{lp} = \langle H_p\rangle - \sum_{i=2}^{N}\bar{h}^n_{ip}$$
$$\bar{u}^n_{ip} = \frac{\bar{M}^n_{ip}}{\bar{h}^n_{ip}}$$
$$\bar{J}^n_{ip} = \frac{(\bar{M}^n_{ip})^2}{\bar{h}^n_{ip}}$$
$$\bar{R}^n_{jp} = \sum_{k=j+1}^{N}\bar{h}^n_{kp} + \langle h^n_{(N+1)p}\rangle.$$

Then the new values of M_i and h_i $(2 \leqslant i \leqslant N)$ are

$$M^{(n+1)}_{ip} = M^n_{ip} - \Delta t\left\{\delta_x(\bar{J}^n_{ip}) + \langle\bar{h}^n_{ip}\rangle\sum_{j=0}^{i-1}\left[\frac{g\rho'_j}{\rho_0}\,\delta_x(\bar{R}^n_{jp})\right] + C_D\sum_{\substack{j=i-1\\ 1\leqslant j\leqslant N}}^{i+1}\langle\bar{u}^n_{ip} - \bar{u}^n_{jp}\rangle\langle|\bar{u}^n_{ip} - \bar{u}^n_{jp}|\rangle - \delta_x(D^n_{ip})\right\}$$
$$+ \Delta t\,\frac{\langle\bar{h}^n_{ip}\rangle}{H_p}\left\{\sum_{l=1}^{N}\left[\langle\bar{h}^n_{lp}\rangle\sum_{j=0}^{l-1}\left[\frac{g\rho'_j}{\rho_0}\,\delta_x(\bar{R}^n_{jp})\right] + \delta_x(\bar{J}^n_{lp}) - \delta_x(D^n_{lp})\right] + \frac{dF^{(n+\frac{1}{2})}}{dt}\right\}, \tag{A3}$$

$$h^{(n+1)}_{ip} = h^n_{ip} - \Delta t[\delta_x(\bar{M}^n_{ip}) - \delta_x(E^n_{ip})]. \tag{A4}$$

REFERENCES

Davis, R. E., 1969: The two-dimensional flow of a stratified fluid over an obstacle. *J. Fluid Mech.*, **36,** 127–143.

Drazin, P. G., and D. W. Moore, 1967: Steady two-dimensional flow of fluid of variable density over an obstacle. *J. Fluid Mech.*, **28,** 353–370.

Farmer, D. M., and J. D. Smith, 1980: Tidal interaction of stratified flow with a sill in Knight Inlet. *Deep Sea Res.*, **27A,** 239–254.

——, and H. J. Freeland, 1983: The physical oceanography of fjords. *Progress in Oceanography,* Vol. 12, Pergamon, 147–220.

——, and R. A. Denton, 1985: Hydraulic control of flow over the sill of Observatory Inlet. *J. Geophys. Res.*, **90,** 9051–9068.

Geyer, W. R., and G. A. Cannon, 1982: Sill processes related to deep-water renewal in a fjord. *J. Geophys. Res.*, **87,** 7985–7996.

Haury, L. R., M. G. Briscoe and M. H. Orr, 1979: Tidally generated internal wave packets in Massachusetts Bay. *Nature,* **278,** 312–317.

Houghton, D. D., and A. Kasahara, 1968: Nonlinear shallow fluid flow over an isolated ridge. *Commun. Pure Appl. Math.*, **21,** 1–23.

——, and E. Isaacson, 1970: Numerical solutions of nonlinear problems. *Studies in Numerical Analysis, S.I.A.M.*, 21–52.

Huppert, H. E., and J. W. Miles, 1969: Lee waves in a stratified flow. Part 3. Semi-elliptical obstacle. *J. Fluid Mech.*, **35,** 481–496.

——, and R. E. Britter, 1982: Separation of hydraulic flow over topography. *J. Hydraul. Div. ASCE,* **108,** 1532–1539.

Long, R. R., 1953: Some aspects of the flow of stratified fluids. I. A theoretical investigation. *Tellus,* **5,** 42–58.

——, 1954: Some aspects of the flow of stratified fluids. II. Experiments with a two-fluid system. *Tellus,* **6,** 97–115.

——, 1955: Some aspects of the flow of statified fluids. III. Continuous density gradients. *Tellus,* **7,** 341–357.

Miles, J. W., 1968: Lee waves in a stratified flow. Part 1. Thin barrier. *J. Fluid Mech.*, **32,** 549–567.

——, and H. E. Huppert, 1968: Lee waves in a stratified flow. Part 2. Semi-circular obstacle. *J. Fluid Mech.*, **33,** 803–814.

——, and ——, 1969: Lee waves in a stratified flow. Part 4. Perturbation approximations. *J. Fluid Mech.*, **35,** 497–525.

Pinkel, R., 1980: Acoustic Doppler techniques. *Air-Sea Interaction.* F. Dobson, L. Hasse and R. Davis, Eds., Plenum, 171–199.

Richtmyer, R. D., and K. W. Morton, 1967: *Difference Methods for Initial-Value Problems.* Interscience, 405 pp.

Stacey, M. W., 1984: The interaction of tides with the sill of a tidally energetic inlet. *J. Phys. Oceanogr.*, **14,** 1106–1117.

Turner, J. S., 1973: *Buoyancy Effects in Fluids.* Cambridge University Press, 367 pp.

Yih, C.-S., and C. R. Guha, 1955: Hydraulic jump in a fluid of two layers. *Tellus,* **7,** 358–366.

Zedel, L. J., 1985: Evaluation of an acoustic Doppler profiler with application to stratified flow in a fjord. M.Sc. thesis, Dept. of Physics, University of Victoria, 183 pp.